Cracking behaviour of high-strength AA2024 aluminium alloy produced by Laser Powder Bed Fusion

G. Del Guercio [a], D.G. McCartney [b], N.T. Aboulkhair [a,c], S. Robertson [d], R. Maclachlan [d], C. Tuck [a], M. Simonelli [a]

[a] Centre for Additive Manufacturing, Faculty of Engineering, University of Nottingham, Nottingham, NG8 1BB, UK

[b] Faculty of Engineering, University of Nottingham, Nottingham, NG7 2RD, UK

[c] Additive Manufacturing Laboratory, Advance Materials Research Centre (AMRC), Technology Innovation Institute (TII), Masdar City, Abu Dhabi, P.O. box 9636, UAE

[d] Department of Materials, Loughborough University, Loughborough, LE11 3TU, UK

Corresponding author:

Marco Simonelli
Marco.Simonelli@nottingham.ac.uk

Abstract

Most wrought aluminium alloys of the 2000 series are difficult to manufacture by laser powder bed fusion (L-PBF) due to the formation of cracks during building. To date, the effects of processing regimes on crack formation are still not well understood. In this study we performed a detailed microstructural characterisation of crack development in the AlCuMg alloy AA2024 to quantify the extent of cracking and porosity arising from a range of different process parameters. Two samples, produced with different build parameters, were selected for in-depth study by scanning and transmission electron microscopy; these had similar low levels of porosity but high (H - 2.6 ± 0.4 mm/mm^2) and low (L - 1.5 ± 0.3 mm/mm^2) crack densities respectively. Based on distinct morphological features and characteristic length, we differentiate hot cracks from solid state cracks. Hot tears form at high angle grain boundaries and are associated with micron-sized gas pores as well as intermetallic phases in both samples. The solidification and cracking behaviour are modelled with the aid of a Scheil-Gulliver model that includes solute trapping. This approach predicts differences in hot-crack-susceptibilities, due to different solidification velocities, in line with experimental observations. The sample H, of high crack density, also experiences the higher cooling rate, and hence strain rate, which contributes to the greater propagation of cold cracks in the low fracture toughness AA2024. The observation of cracking associated with microporosity and the use of a Scheil-based solidification model, including solute trapping, provide new insights into the complex problem of hot tearing during L-PBF.
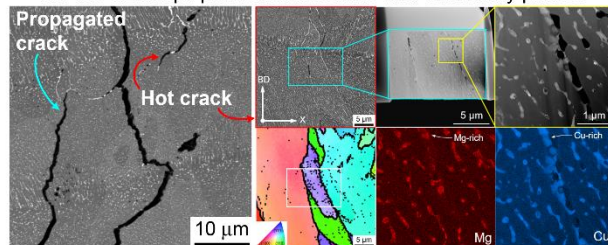
Graphical Abstract

L-PBF of AA2024: *P-v* combinations leading to similar porosity, feature different cumulative crack lengths (CCL)

CCL [mm/mm²]
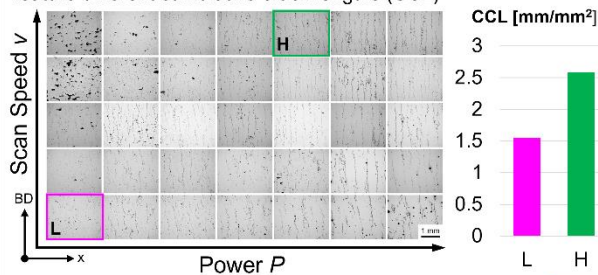
Crack morphology and microstructure
- Hot cracks and cold cracks have distinctive morphologies
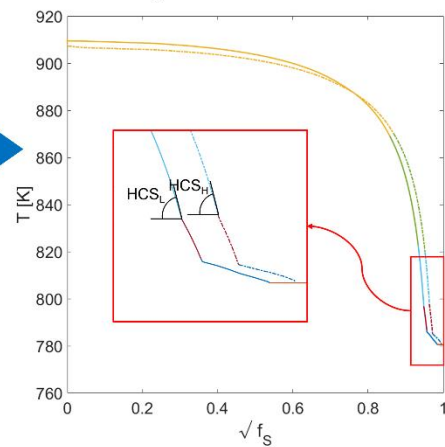- The hot crack tips presents microvoids and secondary phases

WHY?

Nucleation of hot cracks is affected by:
- Phase transformation sequence
- Solidification rate
- Cooling rate

Propagation of hot cracks is affected by:
- Stress state in L-PBF
- Oriented microstructure
- Fracture toughness

Keywords

Additive manufacturing; Aluminium alloys; Cracking susceptibility; Scheil solidification; CALPHAD;

1 Introduction

During the past years, several metal Additive Manufacturing (AM) techniques have generated significant interest for their ability to rapidly fabricate complex parts in a number of high-value materials [1,2]. Specifically, in the last decade the research community has focused on laser powder bed fusion (L-PBF), which has found areas of applications in the automotive, medical and aerospace sectors [3,4]. In the transport industry, aluminium (Al) alloys are in high demand owing to their low density and their suitability for manufacturing structural components. Nevertheless, at present, the proven Al alloys for L-PBF are limited to readily castable alloys, such as those of the Al-Si family (e.g. AlSi10Mg, AlSi7Mg). The vast majority of more attractive high-strength Al alloys from the traditional 2000, 6000 and 7000 series wrought alloys suffer instead from extensive cracking issues during printing due to the typical large solidification range [5], a columnar growth of dendrites and a directional grain structure [6]. The combination of these factors promotes the creation of hot cracks, also known as hot tears, that limit the full consolidation of such materials. These defects are well known to limit the processability of other materials such as high-entropy alloys [7] and Ni-based superalloys [8].

Despite developments in the technology (and associated controls on laser parameters), practical tools to correctly predict densification and mitigate the formation of cracks in high-strength Al alloys during L-PBF remain, therefore, a topic of intense research. The most widely used method to minimise hot cracks in Al alloys during L-PBF is represented by grain inoculation, a technique well-known

from the casting literature, to achieve refined microstructures (also known as grain refined microstructures), which are thought to be useful to avoid the formation of hot cracks [4,5].

A widely used method for grain refinement is the promotion of heterogeneous nucleation via the precipitation of compounds matching the crystallographic lattice spacing and density of the Al-FCC matrix [5]. This must be accompanied by the alloy having a sufficiently large growth restriction factor to permit the nucleant particle to operate in an undercooled zone ahead of the growth front. One example of the application of this strategy is found in the proprietary alloy known as Scalmalloy® [9,10], a specially-modified 5xxx series Al alloy that is resistant to hot cracking during welding and L-PBF. During rapid cooling of molten Scalmalloy®, 0.7 wt.% of Sc is thought to react with Al forming Al_3Sc, a compound highly affine with the FCC-Al matrix. This, in turn, would promote heterogeneous nucleation and consequent overall refinement of the grain structure in the alloy [11–13]. Similar grain refinement mechanisms have been reproduced when Zr was added in concentrations higher than 0.8 wt%. Zr is thought to promote the precipitation of the Al_3Zr – a proven substrate for heterogenous nucleation. Compounds for grain refining can also be added to the base alloys in nano-powder format [5]. Martin et al. [5] proved that addition of 1 vol% Zr nanoparticles was able to mitigate the presence of cracks in the as-build microstructure of both AA7075 and AA6061 due to the heterogeneous nucleation of an equiaxed microstructure promoted by Al_3Zr. Zhang et al. [14] proved the same concept for Al-Cu-Mg when 2 wt% of Zr was added to the base alloy. Often Sc and Zr are both added to a base alloy to improve its processability in L-PBF due to very similar crystallographic matching planes

with the Al-FCC matrix. Jia et al. [15] used 0.79 wt% of Sc and 0.74 wt% of Zr to design a crack-free high-strength alloy characterized by the peculiar equiaxed microstructure promoted by heterogeneous nucleation. The literature offers multiple examples where Sc, Zr and other compounds, such as Ti and TiB_2, are added to several high-strength Al based alloys to form new constitutions directly at the point of L-PBF manufacture [16–21].

These research efforts are, however, associated to high material costs and may result in difficulties for large scale implementation. Moreover, entirely new alloys (other than the commercially available ones) require extensive qualification, in turn potentially limiting the L-PBF technology's uptake.

Of the commercially-available wrought alloys, one of the most attractive alloys for use in L-PBF is AA2024 because of its potential to offer high ultimate tensile strength (360÷515 MPa) and reasonable elongation at failure (6÷20 %) [22]. However, previous research efforts have shown conflicting results in terms of its processability. The consolidation behaviour of AA2024 in L-PBF conditions has been, for example, studied by Gharbi et al. [23]. They found that crack-free AA2024 components can be obtained on a continuous laser system using a power of 80W and a scan speed of 0.30 m/s. Nevertheless, this work lacks a precise interpretation of the mechanisms that enabled the suppression of cracks. Tan et al. [24] showed that, at processing regimes capable of minimising porosity, AA2024 suffers from extensive cracking. In more recent work [20], the authors showed that additions of 1 wt% Ti-nanoparticles can minimise cracking and attributed these improvements to the associated refined (inoculated) microstructures. Similarly, grain refining operated by additions of CaB_6 has been successfully demonstrated

by Mair et al. [25] to minimise cracking. Rasch et al. [26] studied the correlation between hot cracking tendency and solidification behaviour, highlighting the correlation between grain structure morphology and crack density. Despite these efforts, the mechanisms leading to the extensive cracking presence in high-strength Al alloys are not comprehensively understood. Moreover, the effects of the processing parameters need to be fully understood to discuss a material's tendency of forming cracks under L-PBF regimes.

The aim of the present research is to study the solidification of AA2024 and to understand why different processing conditions that lead to comparable optimal relative densities produce significantly different cracking behaviours. To answer this research question, first, we present a microstructural characterisation methodology based on optical microscope image segmentation to differentiate and analyse defects, such as pores and cracks. We then use this approach to quantify the microstructural variations obtained within the range of process parameters yielding minimum porosity. Secondly, we identify two processing conditions minimizing porosity but showing different cracking intensities. The hot cracks' nucleation tendency is then discussed with the aid of site-specific TEM analysis conducted at the tip of a hot crack, hot tearing criterions and solidification paths evaluated using Scheil-Gulliver models considering solute trapping. The use of these newly implemented segregation models provides new insights on the difference in hot-crack-susceptibility in a material processed with two different laser processing speeds. On the other hand, the propagation of hot cracks is discussed as a function of the specific combination of process parameters adopted for fabrication. An understanding of these complex and interconnected

mechanisms leading to the observed extensive cracking in high-strength Al-alloys is of paramount importance, as it will lead to the development of a new practical methodology to identify and design high-strength Al-alloys for L-PBF.

2 Materials and methods

2.1 Powder feedstock and L-PBF processing

AA2024 aluminium alloy powder with the nominal composition shown in Table 1 was procured from TLS Technik GmbH & Co. The composition of the powder was measured using Inductively Coupled Plasma Optical Emission Spectroscopy (ICP-OES) and results are also given in Table 1. A Hitachi TM3030 SEM was used to analyse the morphology of the powder while its particle size distribution was measured using a Mastersizer 3000 from Malvern Panalytical (Figure 1). The powder had a near-spherical morphology, typical of gas atomisation, and the size analysis revealed that the powder is characterised by D10, D50 and D90 values of 29.5 µm, 42.1 µm and 59.6 µm, respectively.

Table 1: Nominal and measured chemical composition of the AA2024 alloy procured from TLS Technik GmbH & Co.

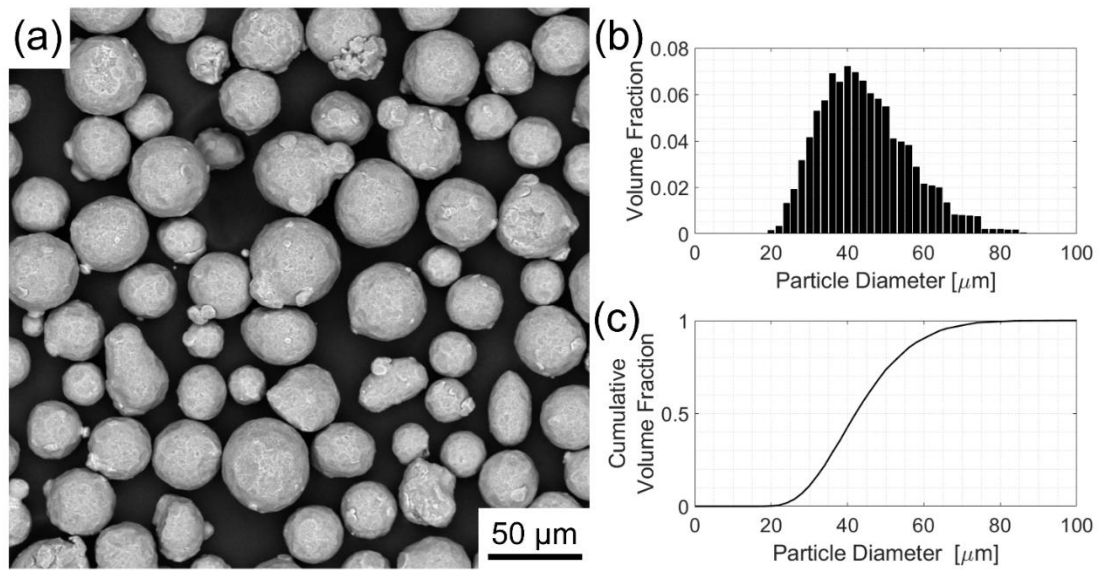|	Element [wt%]								
	Si	*Cu*	*Mg*	*Mn*	*Fe*	*Ti*	*Cr*	*Zn*	*Al*
Nominal composition	≤ 0.50	$3.80 \div 4.90$	$1.20 \div 1.90$	$0.30 \div 0.90$	≤ 0.50	≤ 0.10	≤ 0.10	≤ 0.25	Bal.
Measured composition	0.36	4.57	1.34	0.98	0.12	< 0.02	< 0.02	< 0.02	Bal.

Figure 1: (a) Secondary electron microscope (SEM) image showing the morphology of the AA2024 powder; (b) particle size distribution and (c) cumulative particle size distribution.

Prior to L-PBF processing, the powder feedstock was dried at 70 °C for 24 h. Samples were manufactured using a Renishaw AM400 equipped with a 400 W ytterbium fibre laser. During the process, the L-PBF chamber was maintained under an Ar atmosphere with an oxygen level below 400 ppm to minimise oxidation. In order to reduce thermal expansion and thermal gradients in the samples, the AA5053 aluminium building platform was kept at the highest permitted temperature of 170 °C. Cubic samples with a 10 mm edge were produced to study the microstructure and investigate the formation of features such as, pores and cracks. The samples were produced with a powder layer thickness of 30 μm, using a meander scan strategy with a rotation angle of 67° and a 120 μm hatch distance. In total, 35 unique combinations of power (P) and scan speed (v) were used to produce samples with various processing conditions – Table 2.

Table 2: Range of powers and scan speeds used to fabricate the AA2024 samples.

Parameters	Values
Power [W]	180, 200, 220, 240, 260, 280, 300
Scan speed [m/s]	0.50, 0.75, 1.00, 1.25, 1.50

2.2 Microstructural characterisation of L-PBF samples

In order to quantify the internal defects, the samples were cut parallel to the building direction (BD) and then mounted and polished according to standard practice with a final polish of colloidal silica. A Nikon Eclipse LV100 ND microscope was used to obtain optical micrographs of a plane parallel to the BD which were afterwards analysed to quantify the presence of defects using the developed methodology described in Appendix A.

The phases present in the microstructure were identified using a combination of X-ray diffraction (XRD) and microscopy. A Bruker D8 Advance Da Vinci with a Lynxeye 1D detector was used for XRD analysis of the as-received powder and polished LPB-F samples. Data were acquired with a step size of 0.02° and a step time of 4 s scanning between $2\theta = 15°$ and $2\theta = 90°$. The detected diffraction peaks were then identified in the Bruker software Diffrac.EVA with the aid of the ICDD database PDF+2.

Electron microscopy was carried out using a range of instruments. A xenon-plasma Focused Ion Beam (FIB), Helios G4 He+ pFIB (Thermofisher Scientific formally FEI) equipped with a symmetry Electron Backscatter Diffraction (EBSD) and Ultim Max 170 Energy Dispersive X-ray (EDS) detectors (Oxford Instruments), was utilised

for the collection of EBSD data and backscattered electron images. It was also employed for the preparation of electron transparent (150 nm thick) transmission electron microscope (TEM) lamellae from the region of a crack tip that formed due to hot tearing. Xenon pFIB was used as xenon, unlike gallium, is known not to alloy or form intermetallics with aluminium. This allows higher confidence in the EDS results recorded [27]. Raw EBSD data were post-processed in Matlab with the aid of the MTEX toolbox. Orientation mismatch of 8° was used as a threshold to segment the grain structure. The colour legend of all the EBSD maps was set so that the {100} family of directions of the Al-FCC matrix was aligned to the BD. Ellipse fitting was used to approximate grain size in the plane parallel to the BD. The average minor and major axis were used to evaluate the average width and length of columnar grains. On the other hand, grains in the plane perpendicular to the BD were approximated with circles to evaluate their average diameter. Additionally, the grain boundary (GB) misorientation was used to characterize the cracking interface.

TEM imaging was performed using a FEI Tecnai F20 field emission gun scanning transmission electron microscope (FEG-STEM) operated at 200 kV. The TEM was equipped with Oxford Instruments Energy Dispersive X-ray spectroscopy (EDS) with a 80 cm^2 sized windowless detector. Bright field (BF) and high angle annular dark field (HAADF) images were recorded along with STEM EDS maps for the elements of interest.

2.3 Thermodynamic calculations

The CALPHAD approach using Thermo-Calc™ version 2021b [28] was applied to predict the AA2024's solidification path, phase nucleation sequence, volume

fraction and phase composition. Specifically, the calculations were performed using the Scheil-Gulliver micro-segregation model using the TCAL6 database [29] which was developed for Al alloys. The solidification simulations were performed in both classic Scheil-Gulliver conditions (assuming infinite fast diffusion in the liquid, no diffusion in the solid and presence of thermodynamic equilibrium at the interface) and Scheil-Gulliver conditions contemplating the presence of solute trapping. Differently from the prior, this last case contemplates changes of the partition coefficient k due to higher solutes retain in the Al-FCC matrix. Based on the evaluated solidification paths and segregation profiles, the hot-crack-susceptibility of AA2024 under different processing regimes is discussed.

3 Results

3.1 Densification behaviour of AA2024 in L-PBF

Figure 2 (a) shows representative micrographs, in a plane parallel to BD, corresponding to the specimens obtained with the parameter sets investigated. It can be seen that varying the combinations of P and v had a significant effect on porosity as well as a distinguishable effect on the formation of cracks. These features are known to form a complex 3D network, difficult to visualize and investigate using simple 2D imaging techniques. Nevertheless, since this study focuses on comparing crack intensities found at different processing conditions, the use of OM and SEM micrographs provides enough information to conduct this comparison. Figures 2 (b) to 2 (d) present higher magnification images of these characteristic features. Nevertheless, for each combination of process parameters employed, the cracks were nearly straight and always parallel to the BD, as widely reported in the literature [5,20,30]. Additionally, the presence of small pores, thought to be gas pores, was detected in each processing condition analysed. A representative example for the samples produced using low P and high v (180 W and 1.50 m/s) is presented in Figure 2 (b). This specific condition is seen to be characterized by the presence of large irregular pores, typically associated with processing conditions where lack-of-fusion porosity dominates [24]. Additionally, it was observed that lack-of-fusion porosity was often interconnected by cracks. On the other hand, the outcome of using high P and low v (300 W and 0.50 m/s) can be seen in Figure 2 (c); analogous microstructures were observed in specimens manufactured at similar conditions of high P and low v. This sample was

characterized by the presence of large circular pores that are typically believed to arise as a result of keyhole formation in the melt pool [24]. In this processing regime, cracks were also seen as well as the keyhole type pores. Under the 260 W and 1.50 m/s processing conditions, lack-of-fusion and keyhole porosity were both minimised, as demonstrated in Figure 2 (d). Similar microstructures were observed in samples produced with other P-v combinations in which only small micro-pores were detected. However, under these conditions, cracks were still apparent. Therefore, these results indicate that there is a trade-off between minimising porosity and cracking presence. Additionally, cracks were well-aligned with the BD and occurred as semi-continuous chains. These features will be fully characterised in Section 3.3.
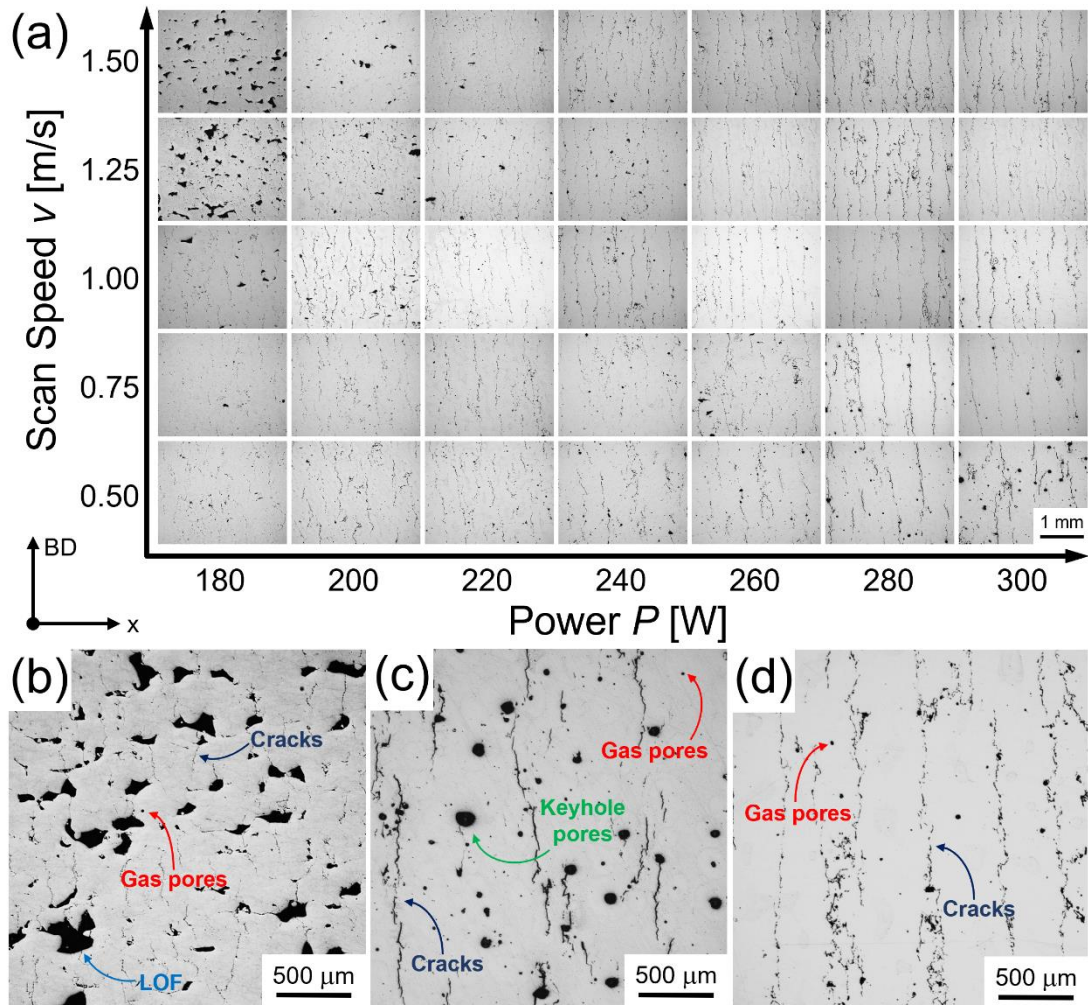
Figure 2: (a) Optical micrographs parallel to the BD of all the P-v combinations experimentally investigated in the present study. (b) shows a typical microstructure of sample manufactured at 180 W and 1.50 m/s showing the presence of LOF, gas pores and cracks. (c) 300 W and 0.50 m/s depicting keyhole pores, gas pores and cracks, and (d) 260 W and 1.25 m/s showing the presence of only gas pores and cracks.

Using the image analysis methodology described in 2.2.1, it was possible to quantify and classify defects, as presented in the contour plots in Figure 3 of the porosity, cumulative crack length (*CCL*) and relative density as a function of both *P* and *v*. According to Figure 3 (a), porosity was minimised at two distinct processing

regimes: (i) power of 260 W and scan speed of 1.50 m/s, and (ii) power of 180 W and scan speed of 0.50 m/s. In the remainder of the study, the samples produced in the former and latter processing regimes will be denoted with H and L, respectively. For the sake of clarity, these processing conditions are marked in Figure 3 by a green and a magenta circle, respectively.

The contour plot of CCL in Figure 3 (b) shows a maximum value at the highest scan speed combined with the highest power and a minimum at the highest scan speed paired with the lowest power. At low scan speeds, the CCL assumes intermediate values with minor variations in all the investigated power range. The sample produced in the H processing regime has higher CCL value (2.6 ± 0.4 mm/mm^2) with respect to the one produced in the L processing regime (1.5 ± 0.3 mm/mm^2). The relative density (Figure 3 (c)) of the produced samples (which takes into account both porosity and cracking) was between 92.1% and 97.8% with samples L and H yielding some of the highest density values (97.3$\pm$0.5% for sample L and 96.7$\pm$0.2% for sample H). It is therefore noteworthy that despite either processing regimes H and L allowed similar amounts of porosity, distinctive values of the CCL are observed, suggesting a significant underlying effect of process parameters on microstructure and cracking development. This is discussed in detail in the subsequent section with the aim to identify the critical features controlling the cracking behaviour of the alloy.
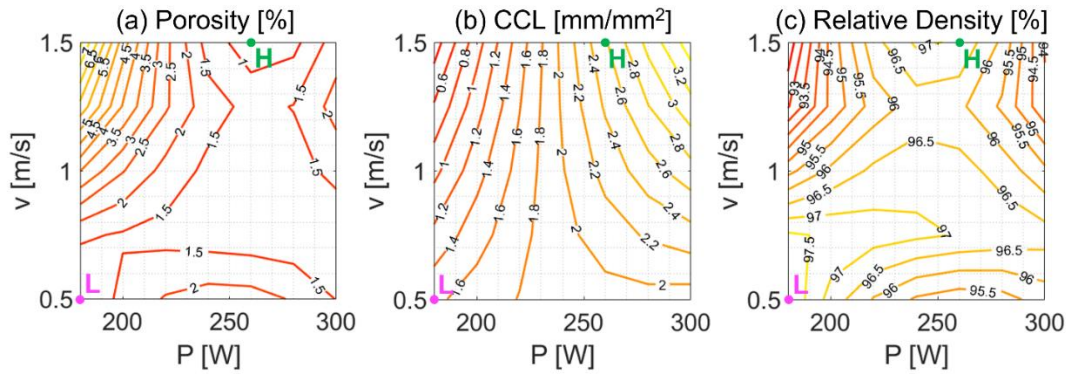
Figure 3: Contour plots showing the trend of (a) porosity, (b) CCL and (c) relative density of samples produced in the investigated processing window as a function of power P [W] and scan speed v [m/s]. H (260 W, 1.50 m/s) and L (180W, 0.50 m/s) processing conditions are highlighted in green and purple, respectively. Units on the colour lines are those of the respective graphs.

3.2 Microstructural characterisation of low porosity samples with different cracking tendencies (L and H)

3.2.1 Phases identification and analysis

XRD analysis was carried out to identify the phases present in the L-PBF samples prepared with conditions L and H, as well as the as-received powder (see Figure 4) as a benchmark. The peaks of the Al-FCC matrix are clearly visible in all specimens. In the powder spectrum, the relative intensity of all the Al-FCC peaks in the investigated 2θ range with respect to the {111} crystallographic plane agrees closely with the ICDD data for pure aluminium. Therefore, no preferred texture is found in the powder. On the other hand, the relative intensities of the {111} and {200} planes were inverted in both of the L-PBF samples. This is commonly attributed to the presence of a preferred {100} crystallographic texture, likely due to the layer-by-layer solidification in L-PBF, and a larger grain size. Several smaller peaks, associated with secondary phases were also present in the XRD

18

diffractograms. Peaks corresponding to Al_2Cu (θ-phase) and Al_3Mg_2 (β-phase) were indexed in all three spectra. Additionally, the ternary compound Al_2CuMg (S-phase) was detected in the powder sample but not in the L-PBF specimens. Generally, the as-received powder showed peaks with lower intensities and larger widths than the as-built alloys. XRD peaks' broadening may happen due to several phenomena, such as, micro-strains caused by high dislocation density or other defects in the crystal structure, small coherent diffracting zone size, chemical lattice parameter's variation caused by inhomogeneous composition in the alloy. Pokharel et al. [31] studied stainless steel manufactured by L-PBF and found that XRD peaks showed broadening because of the higher dislocation density, excluding chemical segregation as a contributing factor. On the other hand, the narrower peaks of the as-built samples suggest that these samples are characterized by a more ordered structure which could arise from the intrinsic thermal treatment associated with multiple passes of the laser beam during L-PBF. Despite these valuable considerations, further studies conducted by either Rietveld analysis or Hall-Williamson method are required to comprehensively differentiate potential causes of peak broadening in AA2024 parts manufactured by L-PBF.

The presence of the observed phases is reported in the literature for AA2024 manufactured by L-PBF [23,25]. The analysis shows conclusive evidence that both specimens H and L contained identical phases.
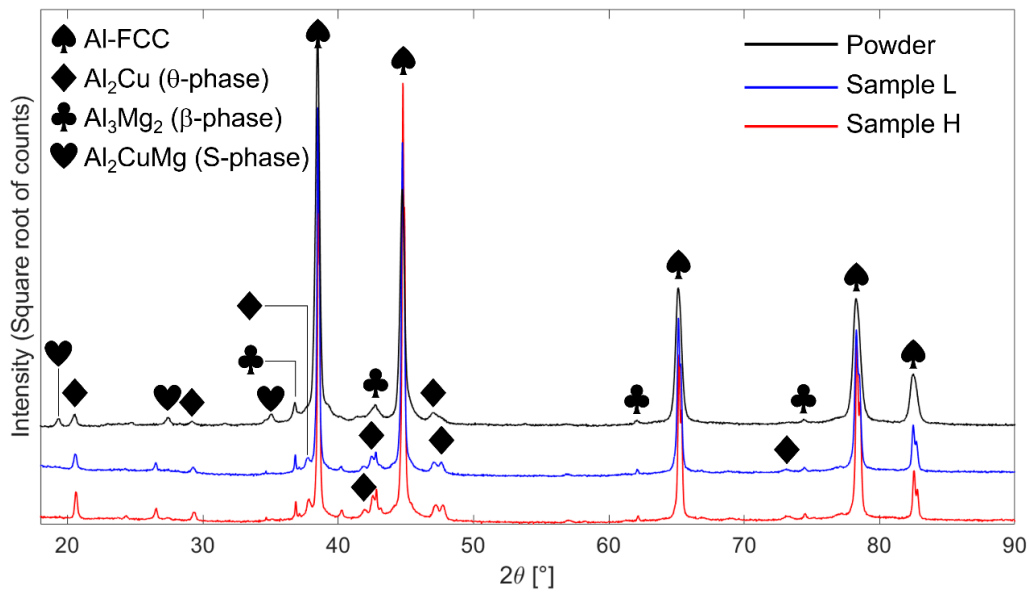
Figure 4: XRD spectra for the powder and samples produced by the L and H L-PBF processing conditions. The S-phase was detected only in the powder sample.

3.2.2 Grain structure and crystallographic texture

Figure 5 shows SEM-BSE images of the microstructure on a plane parallel to the BD of samples L and H. The lower magnification images, Figures 5 (a) and 5 (b), show the melt pool (MP) boundaries, which are traced in yellow. The shape of the melt pool provides insight on the melting regime with which the samples have been manufactured. It was observed that for both processing conditions, the melt pools were relatively shallow. This confirms that specimens were melted, at least predominantly, in conduction mode, supporting the observed porosity trends (no keyhole porosity was detected in these processing conditions). Columnar grains elongated along the BD formed under both processing conditions (Figure 5). Figure 5 (c) and 5 (d) depict, at higher magnification, the microstructure in the vicinity of the melt pool boundaries. The substructure in both specimens is

20

characterized by a fine-scale cellular/dendritic solidification morphology, as typically reported for a variety of Al alloys [5,20,23,24,32] produced by L-PBF. Intercellular/dendritic regions comprise secondary phases, which appear in Figure 5 with a distinctive brighter contrast due to the higher mean atomic number. The apparent aspect ratio of the cells varied depending on the location within the melt pool (boundary, centreline). They appeared coarser in the vicinity of the melt pool boundaries, which is probably due to partial remelting of the solidified melt pools with subsequent laser beam passes. The average cell width was measured at the melt pool boundaries considering 10 adjacent cells. In this area, these substructures grew parallel to each other with their axes aligned with the direction of the heat. At the MP boundaries, a difference in cell width (λ) was observed between samples H and L. The former was characterized by an average cell width of 0.62±0.05 μm, which is slightly smaller than the L sample (0.86±0.05 μm).
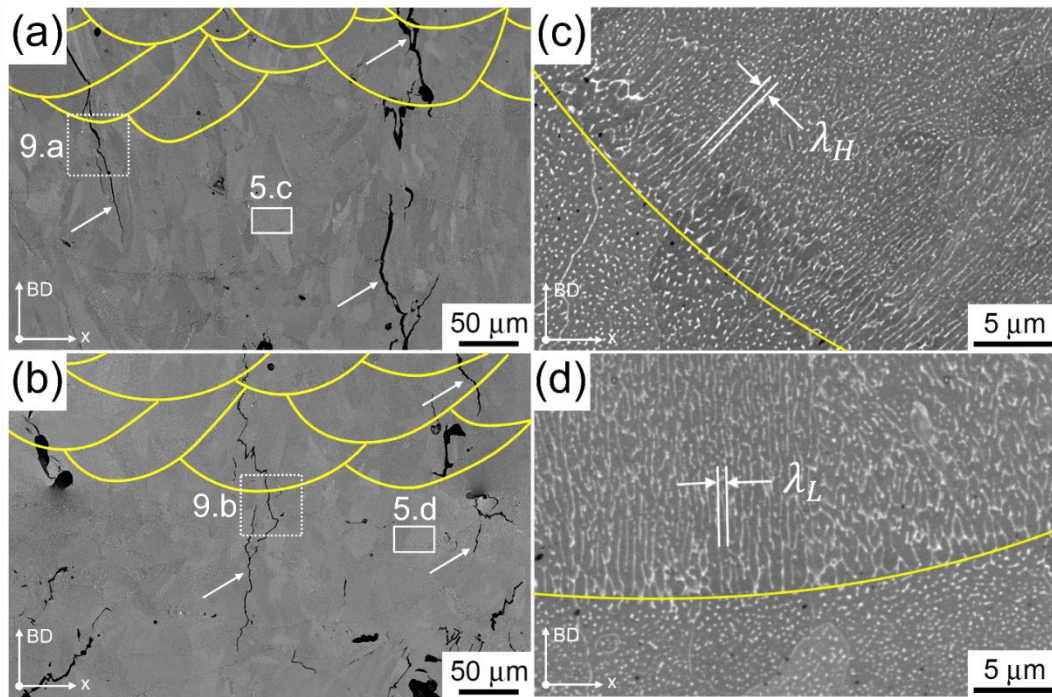
Figure 5: SEM/BSE images of the samples produced by the H (a-c) and L (b-d) processing conditions in the plane parallel to the BD. The melt pool boundaries are indicated by the yellow lines. Micrographs (c) and (d) are site specific details taken from the solid boxes of (a) and (b), respectively. (c) and (d) show the melt pool boundaries and its characteristic dendritic solidification mode. The dotted boxes in (a) and (b) depict the microstructure in the vicinity of the cracks which will be discussed in Figure 9.

EBSD-derived data were used to analyse the crystallographic texture of samples H and L and identify differences in the grain structure and morphology. The EBSD maps in the planes parallel and perpendicular to the BD are presented in Figure 6. In the plane parallel to the BD of both specimens, grains are seen to be elongated along the BD with their main axes tending to align with the main (vertical) heat loss direction (Figures 6 (a) and 6 (b)). As the grains' lengths (which was in the order of 100 μm) exceed those of the melt pools, grains apparently grew epitaxially and span multiple layers, as widely reported in the L-PBF literature [5,20,26]. On the plane perpendicular to the BD, grain appeared with a more evident equiaxed morphology (Figures 6.(c) and 6.(d)). Grain size quantification on

22

these planes showed that the grains in both L and H processing regimes were characterized by a grain diameter of 15.55±14.90 μm and 14.07±12.55 μm. Thus, it can be concluded that the morphology and size of the grains in sample L and H were similar.
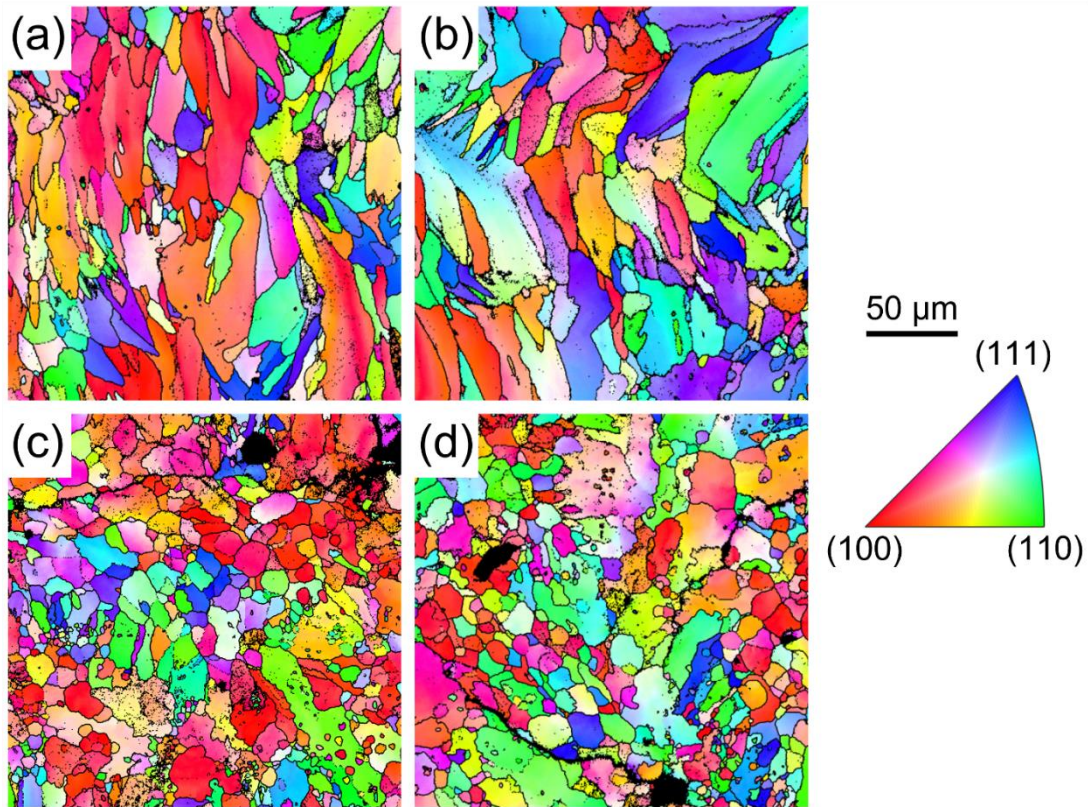

Figure 6: Inverse pole figure (IPF) maps of samples H (a,c) and L (b,d) evaluated for both the planes parallel (a,b) and perpendicular (c,d) to the BD. The inset shows the scale bar and the IPF colour key in which the (100) orientation is aligned with the BD.

Figure 7 illustrates the pole figures of the two analysed samples from the vertical plane. Sample H showed a fibre texture, with a dominant texture component in which {100} is aligned to the BD and relatively weak axisymmetric intensities of the {111} planes around the BD (Figure 7 (a)). On the other hand, a weak fibre

texture was noted in the sample produced under processing condition L (Figure 7 (b)).
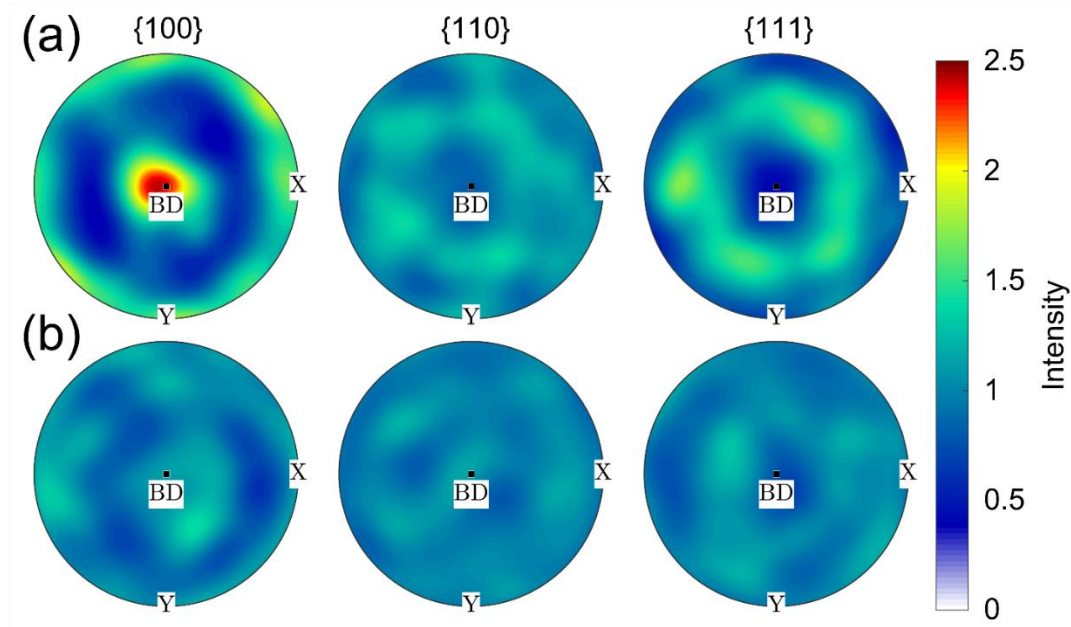

Figure 7: Pole figures of (a) sample H and (b) sample L evaluated in the plane parallel to the BD. Sample H showed the presence of a fibre texture whereas a texture aligned to the BD was not detected in sample L.

The distribution of the grain boundary misorientation angle for both H and L samples is plotted in Figure 8. The grain boundaries' misorientation was found between 15° and 62° for both sample H and L. The prior showed a slightly higher GB misorientation between 26° and 34° with respect to the latter. Although cracks were almost exclusively found to be inter-granular, cracking was observed along a wide range of grain boundary misorientation angles.
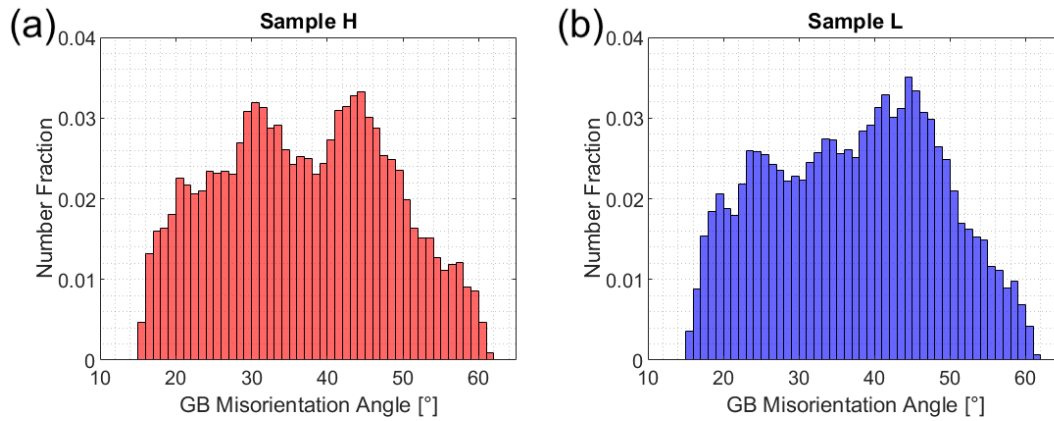
Figure 8: Distribution of the grain boundary misorientation angles evaluated for the (a) sample H and (b) sample L in the plane parallel to the BD.

3.3 Crack morphologies and associated microstructural features

The high magnification SEM images in Figures 9 (a) and (b) show that both H and L displayed cracks with similar but distinctive morphological features. Both samples contained shorter cracks (10-20 μm) of complex morphology often accompanied by secondary phases (showing as bright contrast) at their tips and in between the exposed torn surfaces. Solid arrows indicate the typical morphology of the short cracks. The distinctive morphology and orientation of these short cracks indicates that these are most likely to be hot tears [33,34]. Long cracks spanning multiple layers are also present in the images and are indicated by dashed arrows. These long cracks, reaching lengths of 500-600 μm or more, have instead a near-linear morphology. These long continuous cracks must have propagated through a number of melt pools and so these are likely to be cracks that have propagated in the solid state (though they might have propagated originally from hot tears).
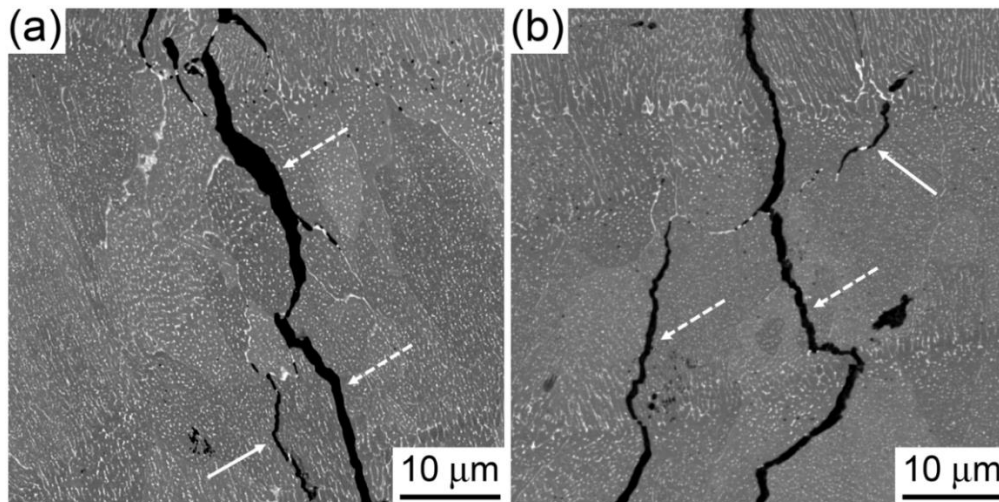
25

Figure 9: SEM/BSE micrographs of samples H (a) and L (b). Solid arrows indicate the typical morphology of the short cracks observed in the builds, while the dashed arrows indicate typical morphology of those cracks that span multiple layers.

EBSD analysis was conducted to gain further understanding of the morphology and crystallographic orientation of grains in the vicinity of the observed short cracks, thought to be hot tears. Figure 10 (a) illustrates the site of interest in a plane parallel to the BD. Incipient hot tears are denoted by the yellow arrows. These features are characterised by a pronounced presence of secondary phases in between crack surfaces. Additionally, the path of the analysed hot tears matches the grain boundaries, as can be seen in Figure 10 (b). Although no particular orientation relationship between the grains surrounding the analysed cracks has been detected, their shape was elongated/columnar, and their main axes were aligned with the BD.
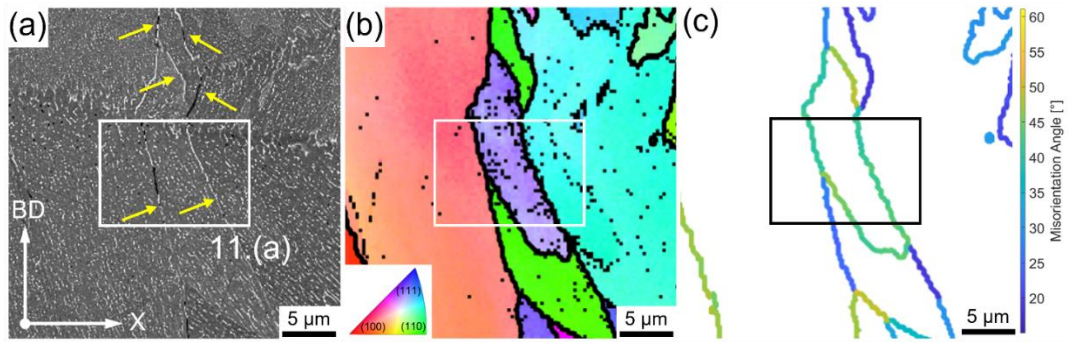
Figure 10: Sample H. (a) BSE micrograph in a plane parallel to the BD showing the analysed short hot tears; (b) IPF map and (c) grain boundary misorientation angle map of the microstructure captured in (a). White boxes in (a,b) and black box in (c) represent the areas where a FIB lift-out thin foil for TEM was taken (Figure 11 (a)).

STEM imaging paired with EDS analysis was conducted to gain a further understanding of the nature of the secondary phases existing along the short cracks (thought to be hot cracks, which have not extensively propagated) present in the microstructure. Figure 11 (a) illustrates the region of the microstructure that was prepared for TEM investigations and this corresponds to the white box region shown in Figure 10 (a). Figure 11 (b) shows a HAADF-STEM micrograph of the microstructure surrounding a fine crack tip. This micrograph shows that the crack (highlighted by solid arrows) opens along the solidification cell boundaries. Moreover, submicron-sized globular pores (highlighted by dashed arrows) were found within the grain in between dendrites. These features are thought to be gas pores that may have been originated either from gases trapped within the melt pool or from residual porosity in the powder [35]. Additionally, the analysis reveals the presence of sub-micron precipitates, ranging from 50 nm to 400 nm in width.

Figures 11 (c-h) depict the EDS maps corresponding to Figure 11 (b). It was observed that a portion of these precipitates are Cu-rich. These particles are believed to be the Al_2Cu phase detected by XRD. EDS maps also revealed the presence of Mg-rich precipitates, which in turn might correspond to the β-Al_3Mg_2 phase detected by XRD. Additionally, the investigation revealed the existence of other phases embedded in the Cu-rich matrix, such as, Si-rich, Si-Mg-rich and Fe-Mn-Si-rich phases in close-proximity to Al_2Cu and Al_3Mg_2. Although the cited compounds were found in all the areas of the studied microstructure, a difference in size and shape can be observed. Analysing these EDS maps, it is clear that the crack is characterized by a increased presence of Al_2Cu with respect to regions far away from the tip. Moreover, the Fe-Mn-rich phases appeared coarser with a better-defined globular shape. Despite not being detected by the XRD analysis, Fe-Mn-rich compounds are thought to be $Al_{15}(Fe,Mn)_4Si_2$ (also known as α-phase), as discussed in Section 4.1.1. No relevant difference in shape or size was detected for the Al_3Mg_2 phases, that appeared fairly equal at both the crack tip and in the bulk microstructure.
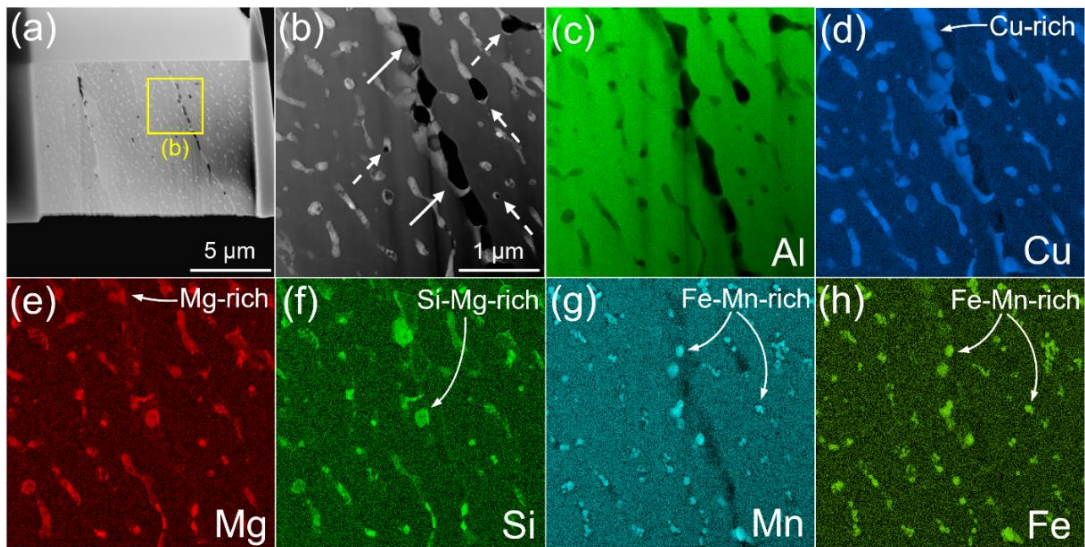
Figure 11: STEM imaging and EDS analysis of sample H. (a) HAADF-STEM of thin foil showing the microstructural overview in the vicinity of the crack investigated and the area where TEM-EDS was carried out (yellow box) (b) HAADF-STEM image presented with the (c-h) corresponding EDS maps of Al, Cu, Mg, Si, Mn and Fe.

4. Discussion

4.1 Crack development in L-PBF of AA2024

4.1.1 Nucleation of cracks under L-PBF regimes

The presence of hot cracks (a.k.a. hot tears) is a well-documented issue limiting the processability of high-strength Al-alloys during L-PBF [5,24–26]. It is known that hot tearing is a cracking mechanism affecting materials that solidify over a large temperature range [36]. In the last stage of solidification, when the volume fraction of solid is above 0.85-0.95 [37], the liquid film of the mushy zone may part due to the high presence of thermal strains associated with the phase transition. It is thus critical to evaluate the solidification path of a given alloy. The shape of this trajectory is influenced by both the composition of the material in analysis and the manufacturing history and can be evaluated using the CALPHAD approach paired

with appropriate micro-segregation models. This requires some considerations. The Scheil-Gulliver model (Equation 1, [38]), widely used to discuss the solidification path of additively manufactured alloys [5,23,26], assumes the presence of thermodynamic equilibrium at the solid-liquid interface, infinitely fast diffusion in the liquid and the absence of diffusion in the solid phase.

$$C_L(1 - k)df_S = (1 - f_S)dC_L \qquad (1)$$

In Equation 1, C_L represents the composition of the liquid, f_S is the fraction of solid, k is the partition coefficient and corresponds to the one evaluated in equilibrium conditions k_e. Nevertheless, in rapid solidification processes, such as, L-PBF, solutes may be "buried" in the solid phase due to the presence of high solidification rates [39]. This phenomenon, known as solute trapping, results in alterations of the partition coefficient at the solid-liquid interface [40–42] which can be described by:

$$k = k_e + (1 - k_e)e^{-\frac{D_i}{R\lambda}} \qquad (2)$$

where D_i is the interface diffusivity, λ represents the interatomic spacing and R is the solidification rate. In modulated processing conditions, this parameter is directly proportional to the laser scan speed following [43]:

$$R = v \cdot \cos \theta \qquad (3)$$

where v represents the scan speed and θ the angle between the dendrites' growth

and the laser directions. This angle has been considered equal to 45° in both cases

with the specific aim of evaluating the solidification rate and the deviation of the

partition coefficient from the equilibrium condition (Equation 2) in a region

located in the rear of the melt pool which is more likely to not be remelted.

Increments of v cause consistent variations of the partition coefficient which in

turn alter the solidification trajectory of a given alloy.

Figure 12 (a) depicts the solidification paths evaluated using the classic Scheil

model and the solute trapping variant with 0.5 and 1.5 m/s. These two last

conditions represent the processing conditions of L and H, respectively. It can be

noted that with respect to the classic Scheil equation, the paths computed

considering solute trapping are indeed shifted towards greater fractions of solid

due to the different alloying elements content trapped in the Al-FCC matrix

(Figures 12 (b-d)). The solute trapping variant predicts a content of Cu, Mg and Si

higher than the ones computed using the classic Scheil model. Moreover, an

increment of solidification speed v causes a higher segregation in the Al-FCC

matrix given by the higher cooling rate [44]. The change of the solidification path

depicted in Figure 12 (a) is crucial to discuss and predict the hot cracking

behaviour of a given alloy. The portion of the solidification path towards the end

of solidification resembles the shape of a columnar dendritic grain near the grain

boundary [45]. Therefore, solidification trajectories shifted towards higher

fractions of solid are expected to have a narrower intergranular channel. This, as

also proven by [7], increases the hot-crack-susceptibility of a given material as it

will be harder for the liquid to percolate and backfill an opening crack. A note of

care should therefore be considered when micro-segregation models that do not assume solute trapping are applied to L-PBF as a change of the solidification path, as depicted in Figure 12 (a), may impacts one's ability to predict the cracking behaviour of the alloy.
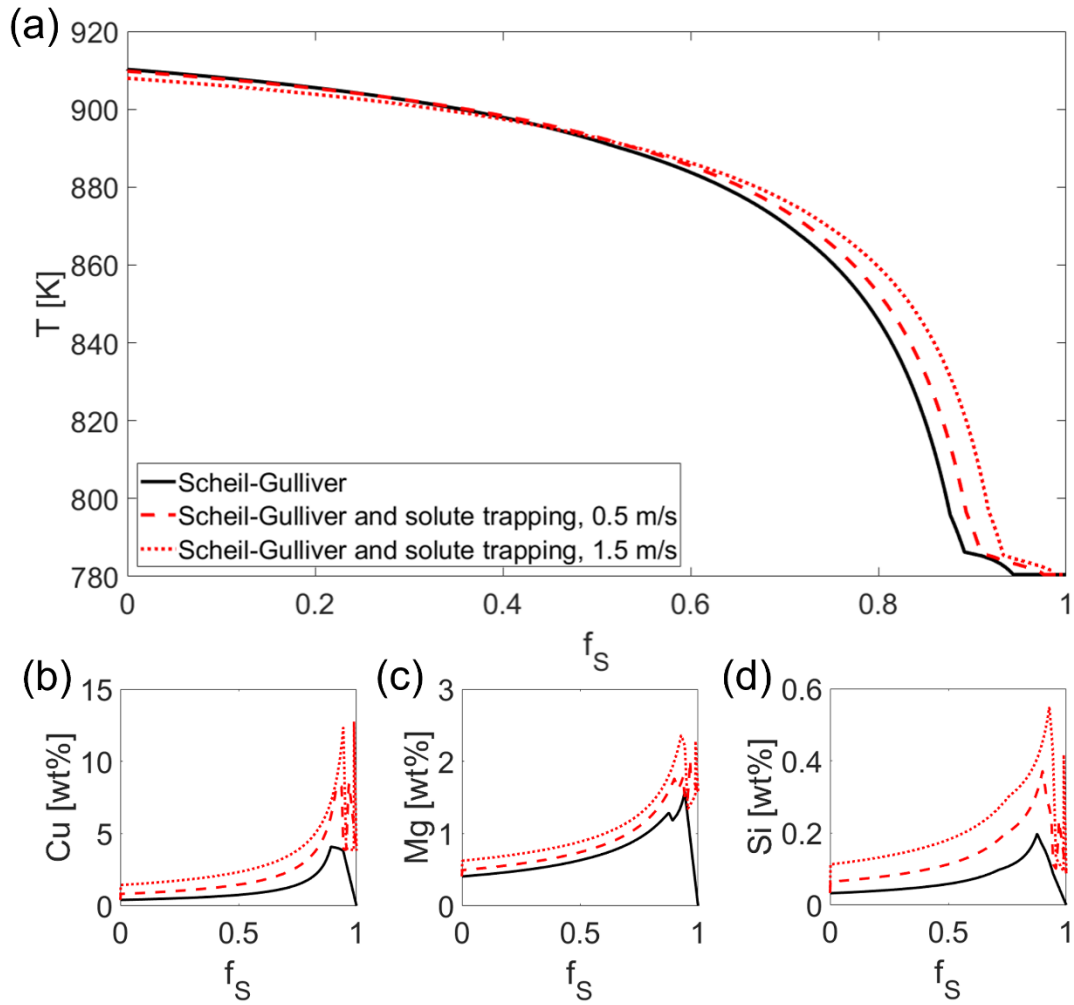

Figure 12: solidification paths of AA2024 evaluated using the Scheil-Gulliver equation and the solute trapping variant with 0.5 and 1.5 m/s (a); solute content of Cu (b), Mg (c) and Si (d) in the Al-FCC phase as a function of the fraction of solid evaluated using the classic Scheil model and the solute trapping variant.

In order to correctly discuss the cracking behaviour of AA2024 using the solidification path depicted in Figure 12 (a), it is useful to compare the phases predicted by Thermo-Calc at the end of solidification with the compounds experimentally found in the microstructure. Table 3 lists the multi-phase regions predicted by Thermo-Calc for the AA2024 alloy under Scheil and solute trapping assumptions. These calculations predict that after the Al-FCC matrix, Al_6Mn is the first secondary phase that precipitates, followed by $Al_{15}(Fe,Mn)_4Si_2$ (α-phase), Mg_2Si, Al_2Cu (θ-phase) and then the S-phase (Al_2CuMg). Apart from the Al-FCC matrix, both the XRD and TEM analyses were able to detect the presence of Al_2Cu and Al_3Mg_2. Additionally, the TEM-EDS maps revealed Si-Mg-rich and Fe-Mn-Si-rich zones in close proximity to the θ and β compounds. These phases are thought to be Mg_2Si and $Al_{15}(Fe,Mn)_4Si_2$. Although we could not detect the presence of the Al_2CuMg and the Al_6Mn phases (neither in the XRD nor TEM analysis), which might be kinetically suppressed by either the fast cooling rates or intrinsic thermal treatment associated with L-PBF, Scheil-Gulliver (with solute trapping) predictions find generally good correspondence to the observed microstructure.

Table 3: List of multi-phase regions predicted by Thermo-Calc under Scheil and solute trapping assumptions for both the H and L processing regimes and the AA2024 alloy.

Multi-phase regions
Liquid + FCC
Liquid + FCC + Al_6Mn

Liquid + FCC + Al_6Mn + $Al_{15}(Fe,Mn)_4Si_2$
Liquid + FCC + $Al_{15}(Fe,Mn)_4Si_2$
Liquid + FCC + $Al_{15}(Fe,Mn)_4Si_2$ + Mg_2Si
Liquid + FCC + $Al_{15}(Fe,Mn)_4Si_2$ + Mg_2Si + Al_2Cu
Liquid + FCC + $Al_{15}(Fe,Mn)_4Si_2$ + Mg_2Si + Al_2Cu + Al_2CuMg

The solidification path of AA2024 is then considered using established cracking models and parameters in the literature. In the past decades, several theories have been proposed to comprehensively discuss mechanisms that lead to hot cracking [45–49]. Clyne and Davies [46] proposed a hot-crack-susceptibility model based on the consideration of the time during which hot tearing takes place. They proposed an empirical cracking susceptibility coefficient defined as the ratio between the vulnerable time-period t_v and the time available for the stress relief process during solidification t_R. Despite being one of the first attempts of cracking tendency quantification, the Clyne and Davies approach possesses intrinsic uncertainties related to boundaries of the fraction of solid in which one should evaluate both t_v and t_R. A more recent approach was proposed by Rappaz, Drezet and Gremaud (RDG) [47]. The RDG model integrates both the fluid backfilling and the deformation in the mushy zone to describe the nucleation of a hot crack from a cavitation. Following this criterion, a void is formed when the liquid pressure drops below the cavitation pressure p_c. Despite being the first hot tearing model describing cracking nucleation based on a physical concept, Coniglio and Cross [50] demonstrated that cavitation due to pressure drop is unlikely to happen in the mushy zone. These two cracking models are therefore deemed not able to capture

the complex mechanisms occurring in the mushy zone that cause hot cracking. Recently, Kou [45] proposed a new hot tearing criterion based on the consideration of the liquid-solid dynamics occurring in the last stage of solidification, that is the final segment of the solidification path. The model considers the growth of columnar dendrites, which are subjected to tensile deformation perpendicular to their main axis. According to Kou's criterion, hot cracks nucleate between solidifying dendrites when the condition in Equation 4 holds:

$$\left\{ \quad \dot{\varepsilon} \quad > \quad \sqrt{1-\beta}\frac{\sqrt{f_S}}{dT}\frac{dT}{dt} \quad + \quad \frac{d}{dz}\left[(1-\sqrt{1-\beta}\sqrt{f_S})v_z\right] \quad \right\}_{\sqrt{f_S}\to 1} \qquad (4)$$

$$\text{(separation)} \qquad \text{(growth)} \qquad \text{(feeding)}$$

where $\dot{\varepsilon}$ is the strain rate upon cooling, β is the solidification shrinkage, f_S is the fraction of solid in the mushy zone, T represents the temperature and v_z the velocity associated with the liquid backfilling the area in-between dendrites. Following Equation 4, Kou proposed an index to predict an alloy's hot-crack-susceptibility (*HCS* – Equation 5) based on the shape of the solidification path upon cooling (also known as solidification gradient) [45,49]. This parameter is evaluated by the computation of the maximum absolute value of the derivative of the temperature with respect to the square root of the fraction of solid at the last stage of solidification [49], with low *HCS* values considered beneficial against cracking.

$$HCS = \max \left| \frac{dT}{d\sqrt{f_S}} \right|_{\sqrt{f_S} \to 1} \qquad\qquad (5)$$

Figure 13 depicts the solidification paths of AA2024 evaluated under Scheil-Gulliver and solute trapping assumptions and the direct application of Equation 5. Table 4 lists the value of HCS calculated for AA2024 (sample H and L) and other common high-strength Al-alloys. It is observed that AA2024 has a *HCS* value of 2198 K and 2307 K in the L and H processing regimes, indicating, as expected, a significant sensitivity of cracking to the manufacturing history, and the higher propensity of sample H to crack. For a given solidification speed, comparatively to other high-strength Al alloys, such as, AA6061 and AA7075 , AA2024 has the lower hot-crack-susceptibility. Nevertheless, its extensive cracking suggests that *HCS* values in the order of 2000 K are not enough to avoid crack nucleation during L-PBF.

Table 4: values of hot-crack-susceptibility (HCS) for AA2024 (this study, samples H and L) and characteristic high-strength Al-alloys found in the literature.

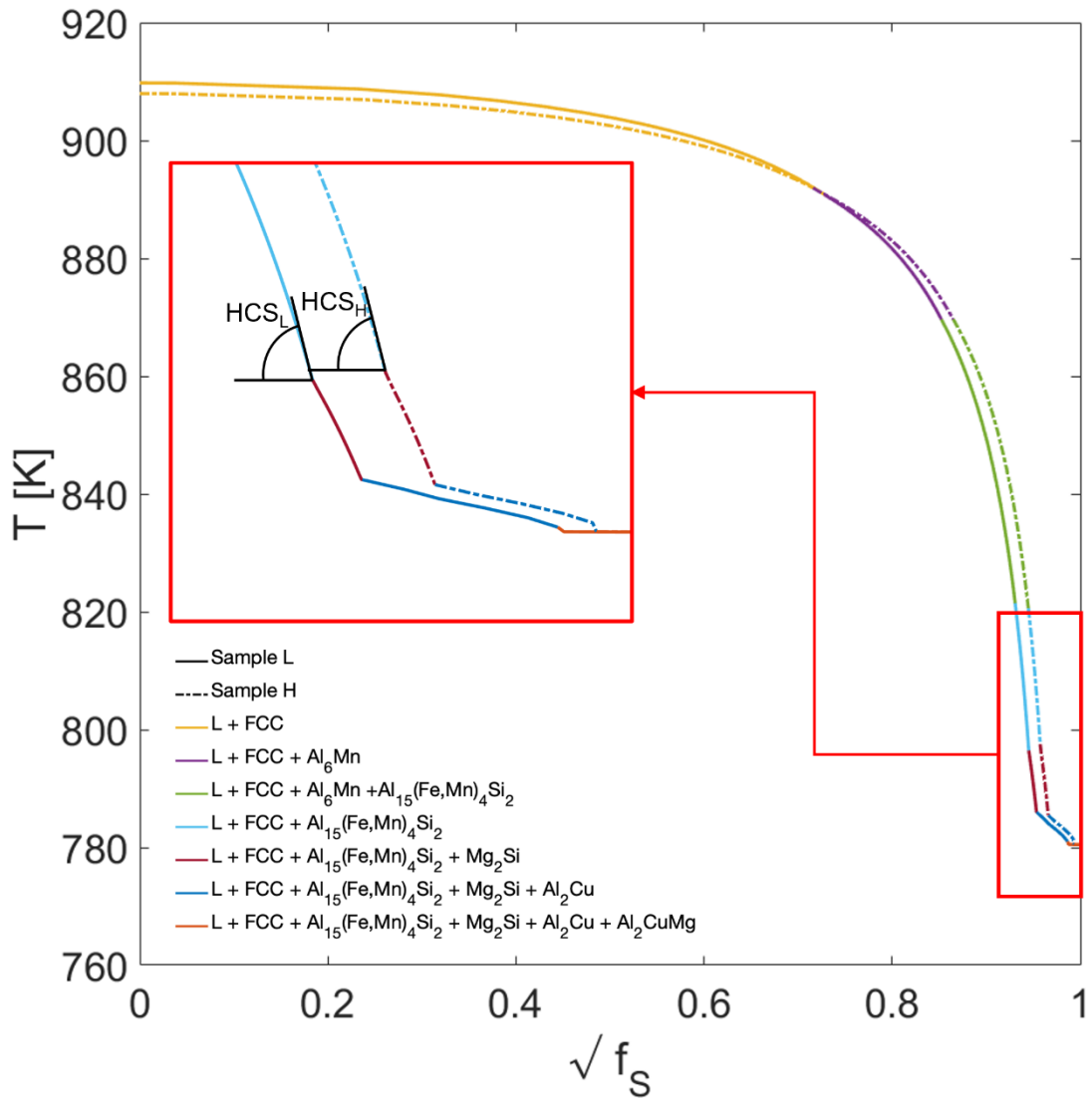| Alloy	HCS [K]
AA2024, sample H	2307
AA2024, sample L	2198
AA6061 [5]	10420
AA7075 [51]	2871

Figure 13: Square root of mole fraction of solid forming in AA2024 using Scheil-Gulliver model of micro-segregation and solute trapping (Thermo-Calc 2020a, TCAL6 database). The plot displays the solidification path of both sample L and H, showing the sequence of the phases that form at the various stages of solidification. The inset depicts the critical region in which the HCS parameter is evaluated.

A note of care should be considered when Sc, Zr and/or Ti are added to the base alloy; the addition of these elements promotes the precipitation of compounds at the beginning of solidification characterized by a high crystallographic matching

with the Al-FCC matrix, promoting the presence of an equiaxed microstructure achieved via heterogenous nucleation. In this case, the solidification path of the resulting alloy does not significantly change towards the end [5] and as a result the HCS of the non-refined and the grain-refined alloy is not expected to change. Additionally, other microstructural features not contemplated in Kou's criterion and in HCS influence the nucleation of hot cracks. Chandra et al. [8] demonstrated that in Ni-based superalloys hot cracks are more prone to be found in correspondence of divergent grain boundaries. Sun et al. [7] showed that in high-entropy alloys, in opposition to what has been found in the present work, the hot cracks' surfaces are not characterized by solutes' segregation. This highlights the intricate and vast phenomena that affects hot tearing and the need to comprehensively study microstructure evolution when discussing the hot-crack-susceptibility of a specific alloy. Although the *HCS* parameter is not able to comprehensively capture the dependence of hot cracking on the microstructure, it offers a good perspective on the processability of a given alloy.

Noteworthy is also a consideration of how processing conditions and the thermo-mechanical behaviour of the alloy investigated can impact hot-cracking nucleation (separation term in Equation 4). The nucleation of hot cracks is largely influenced by the strain rate developed in the mushy zone, which, during L-PBF, is located at the melt pool tail's periphery. In this area, strains perpendicular to the scanning direction develop as a consequence of the limited shrinkage and contraction of the material [52]. Drezet et al. [53] proposed the following expression to evaluate the strain rate at the rear of the melt pool created by a moving laser:

$$\dot{\varepsilon} = -\alpha \dot{T} \tag{6}$$

where α represents the thermal expansion coefficient while $\dot{T}$ is the cooling rate. Clearly, the high cooling rates associated with rapid solidification processes such as, L-PBF, promote the development of large strain rates, which favour the nucleation of hot cracks.

The cooling rate at the melt pool's tail can be estimated using the following [54]:

$$\dot{T} = 2\pi k (T_{sol} - T_0)(T_{liq} - T_0)\frac{v}{AP} \tag{7}$$

where k is the thermal conductivity, A is the absorptivity, T_0 represents the platform temperature while T_{sol} and T_{liq} are the solidus and liquidus temperatures, respectively. For a given alloy, it can be evinced that cooling rates and strain rates are directly affected by the ratio between the scan speed and power. Sample H and L have been produced with v/P ratios of 5.77 and 2.78 mm/J, respectively. Consequently, the cooling rate at the melt pool's tail experienced by sample H was significantly higher than in the case of sample L. This difference is in agreement with the characteristic dendrite width measured in Section 3.2. The cell width λ value is indeed influenced by the cooling rate following the relationship reported by Matyja [55] for rapidly solidified Al-alloys, according to which the increase in $\dot{T}$ is paired by a decrease in dendrite width. This might also explain why sample H is characterized by higher cracking intensities than sample L. As a result, to minimise the nucleation of hot cracks, processing regimes characterised by low laser scan

speeds and low *v/P* ratios are advised. Evidence that in these regimes cracks can be minimized or inhibited is ample [56–58]. Nevertheless, these processing conditions are paired with high energy densities, which may result in the formation of keyhole porosities, and are characterized by values of scan speed not commercially competitive using currently available laser beams. The need to change processing parameters to reduce the hot tears' nucleation tendency of a given material is a well-known practice also in traditional manufacturing techniques. M'hambdi et al. [59] illustrated indeed that a reduction of the casting speed is able to reduce the presence of hot cracks in materials processed by DC casting.

4.1.2 Propagation of cracks during L-PBF of AA2024

The extensive cracking behaviour in Figure 5 is thought to be the result of solid-state propagation (cold cracking) of hot tears. The *CCL* can therefore be used as an effective parameter to quantify the overall cracking propagation behaviour in the alloy. The first attempt to understand the mechanisms associated to the propagation of defects was proposed by Griffith [60] who studied crack growth in brittle materials. This theory was later extended by Orowan [61] to crystalline materials considering the presence of plastic deformation occurring at the tip of the crack. The growth of the crack at its tip is controlled by the critical stress intensity factor via [62]:

$$\sigma_c = \frac{K_{Ic}}{\sqrt{\pi a B}} \qquad (8)$$

where σ_c is the critical stress needed to propagate the crack, K_{Ic} is the fracture toughness of the alloy, a represents the crack length and B is a dimensionless geometrical factor. Compared to steels or Ti-alloys, Al-alloys show relatively low values of K_{Ic} [63]. Additionally, the fracture toughness of a material is influenced by temperature and microstructural features [62]. The presence of long grain boundaries characterized by segregation may further lower the fracture toughness of AA2024, promoting crack propagation. Despite the extensive cracking found in the microstructure is thought to be the result of a solid-state propagation, hot tears nucleated in previous layers may propagate in the current one when they are intercepted by the fusion boundary. In this case, the characteristic length of the crack a increases, resulting in a reduction of the critical stress σ_c necessary to propagate the defect.

For a given alloy of fracture toughness K_{Ic} one ought to minimise the stress state imparted by the manufacturing process to reduce cold cracking. It is well-known that L-PBF materials are inherently affected by high residual stresses, which develop as a consequence of the high thermal gradients across the melt pool boundary [64]. Nevertheless, stress distribution during L-PBF is primarily affected by the melt pool's aspect ratio and, in turn, by the laser power and speed used to manufacture the parts [65]. For example, Mukherjee et al. [66] proved that residual stresses are reduced by adopting processing windows characterised by low v/P ratios. The different *CCLs* measured in the samples H and L can be rationalised considering a likely different stress state in the materials. It is noteworthy that other process parameters may reduce the formation of stresses and the propagation of cracks. Scan strategies that minimise the scan vector length,

such as the checkerboard island or "stripe" strategy, which anecdotally mitigate the presence of large cracks could be explained with similar reasoning [65]. Additionally, an increase in the platform temperature T_0 could lower the thermal gradients across the melt pool boundaries (particularly in low melting point alloys such as those of Al) [64,67].

Finally, one should consider the potential fracture toughness anisotropy associated with L-PBF microstructures. As expected, we observed cracks developing along columnar grain boundaries, weak microstructural features owing to the presence of segregates and brittle precipitates. Recent research has elucidated the importance of controlling grain boundary segregation to maximise dendrite bridging and heal hot tears [68].

EBSD analysis in both planes parallel and perpendicular to the BD revealed that most grains were characterised by high angle grain boundaries (HAGBs) with misorientation angles greater than 15°. It is thought that HAGBs are more prone to hot cracks due to lower coalescence temperature (the temperature of bridging initiation between adjacent dendrites) and predominance of HAGB cracking is a well-documented issue in the Ni-based superalloys [69,70]. It is therefore plausible that cracks, once nucleated, might preferentially grow along these grain boundaries.

4.2 Implications on alloy design to reduce cracking in L-PBF

The analysis of the cracking behaviour of AA2024 in L-PBF conditions has highlighted the presence of both hot tears and cold cracks. Cracking seems, therefore, an issue intrinsically related to the composition of AA2024 and the processing conditions imposed by L-PBF fabrication. The only investigation describing the L-PBF production of crack-free AA2024 samples (Gharbi et al. [23]) reports an incidental higher content of Si (0.78 wt% of Si, as opposed to 0.5 wt%, which is the maximum Si content for nominal AA2024). Silicon addition is a well-reported method to improve the processability of high-strength Al-alloys when processed by L-PBF. Silicon can reduce the alloy's liquidus temperature, introduce a new low melting point eutectic and improve the alloy's fluidity [51,71].

It is noteworthy however, AA2024 and AA2024+Si possess similar values of *HCS* (and thus, at least nominally, similar propensity to nucleate hot cracks). Moreover, Li et al. [32] report the manufacture of crack-free AA7075+Si samples (associated to a *HCS* of 3960 K, thus significantly higher than the *HCS* of the AA2024 in our study). This suggests, as also proposed by Benoit et al. [72], that a single parameter, such as *HCS*, cannot alone capture the complexity of hot-crack susceptibility of high-strength Al-alloys during L-PBF. It is proposed instead that *all* terms of Equation 4 should be assessed in detail. As discussed in Section 4.1, other mechanisms affecting crack nucleation (such as, shape of dendrites, size and morphology of secondary phases at the crack tip, fluidity of the liquid and strain rates associated to specific L-PBF conditions) are not contemplated by the *HCS*

43

parameter but appear to be significant factors affecting the alloy's crack susceptibility.

Finally, mechanical properties of AA2024 are maximized by aging heat treatments with the specific aim of promoting the formation of finely dispersed Al_2CuMg and Al_2Cu [23,73]. Silicon in excess of the standard allowable is likely to cause precipitation of undesirable phases and thus have a poisoning effect (analogous to that reported by Li et al. [32], who describes the occurrence of Mg_2Si instead of a desirable Mg_2Zn in AA7075).

This sheds light on one of the most challenging aspects of the alloy design in AM. The development of new high-strength Al-based materials for the L-PBF process needs to be conducted bearing in mind not only processability constraints, such as hot-crack-susceptibility and residual stresses, but also design constraints, such as precipitates' nature and strength. The integration of these two classes of conditions in the alloy development process will enable the formulation of new materials with tailored properties, specifically designed for the L-PBF process.

5 Conclusions

This study investigated the origins of different cracking behaviours of AA2024 in L-PBF. A methodology to identify and then quantify defects arising from L-PBF fabrication is proposed to quantitatively differentiate cracking intensity as a function of laser processing variables. The microstructure is then analysed in detail with the specific aim to provide a comprehensive discussion of the mechanisms leading to the different cracking intensities observed in the printed samples. This required investigation of the microstructural features near hot crack

tips and discussion of the solidification behaviour under different processing conditions with the use of micro-segregation models. The main conclusions are summarised in the following:

1. Although cracking is ubiquitously observed in the printed samples despite these being produced under an extensive range of processing conditions, higher cracking intensity was detected in samples produced using high laser power P and laser speed v. On the other hand, cracking is minimised in samples manufactured with low values of P and v.

2. The study shows the simultaneous presence of hot tears and solid-state (cold) cracks. Hot tears are thought to nucleate during a single melting event. These might then propagate as cold cracks along vertical grain boundaries in the subsequently deposited layers. Specimens with extensive cold cracks result in relative higher cracking density (CCL).

3. Hot tears exhibit a distinct morphology and were found predominantly between grains at high-angle grain boundaries. Site-specific TEM analysis conducted at the hot-crack's tip revealed the presence of an intricate network of secondary phases (Cu- and Fe-Mn-rich) and micropores, suggesting that the latest stages of solidification and micro-defects forming in the melt pool might play a pivotal role in hot crack formation.

4. The solidification of the alloy was then evaluated using Scheil-Gulliver assumptions with and without solute trapping in order to describe how changes to the solute partitioning coefficient due to variation of laser scan speed might affect phase formation and crack susceptibility. An increase in laser scan speed cause enrichment of the Al-FCC matrix with the alloying

elements. As a result, higher HCS values are measured (the maximum solidification gradients also occur at relative higher solid fractions). Increments in laser scan speed result additionally in higher strain rates. Results indicate that there is a trade-off between deposition rates in L-PBF and hot crack susceptibility.

5. Hot cracks propagate in the subsequent solid layers due to the combination of high residual stresses and oriented high angle grain boundaries. These conditions are favoured by a high v/P ratio, columnar grain growth and strong crystallographic texture. Crack propagation can therefore be significantly reduced by changing processing conditions appropriately.

This study provides new insights on the effects of L-PBF processing regimes on hot-crack's nucleation and propagation in high-strength Al-alloys. It is proposed that the complex mechanisms leading to the extensive cracking in such materials cannot be captured by a single parameter, such as, HCS. All the aspects discussed in the present work need to be considered in the development of new practical methodology to design crack-free high-strength Al-alloys specifically tailored for the L-PBF process without the use of grain refiners.

Acknowledgments

References

[1] T. DebRoy, H.L. Wei, J.S. Zuback, T. Mukherjee, J.W. Elmer, J.O. Milewski, A.M. Beese, A. Wilson-Heid, A. De, W. Zhang, Additive manufacturing of metallic components – Process, structure and properties, Prog. Mater. Sci. 92 (2018) 112–224. https://doi.org/https://doi.org/10.1016/j.pmatsci.2017.10.001.

[2] D. Zhang, S. Sun, D. Qiu, M.A. Gibson, M.S. Dargusch, M. Brandt, M. Qian, M. Easton, Metal Alloys for Fusion-Based Additive Manufacturing, Adv. Eng. Mater. 20 (2018). https://doi.org/10.1002/adem.201700952.

[3] M. Garibaldi, I. Ashcroft, M. Simonelli, R. Hague, Metallurgy of high-silicon steel parts produced using Selective Laser Melting, Acta Mater. 110 (2016) 207–216. https://doi.org/10.1016/j.actamat.2016.03.037.

[4] N.T. Aboulkhair, M. Simonelli, L. Parry, I. Ashcroft, C. Tuck, R. Hague, 3D printing of Aluminium alloys: Additive Manufacturing of Aluminium alloys using selective laser melting, Prog. Mater. Sci. 106 (2019) 100578. https://doi.org/10.1016/j.pmatsci.2019.100578.

[5] J.H. Martin, B.D. Yahata, J.M. Hundley, J.A. Mayer, T.A. Schaedler, T.M. Pollock, 3D printing of high-strength aluminium alloys, Nature. 549 (2017) 365–369. https://doi.org/10.1038/nature23894.

[6] K.G. Prashanth, J. Eckert, Formation of metastable cellular microstructures in selective laser melted alloys, J. Alloys Compd. 707 (2017) 27–34. https://doi.org/https://doi.org/10.1016/j.jallcom.2016.12.209.

[7] Z. Sun, X.P. Tan, M. Descoins, D. Mangelinck, S.B. Tor, C.S. Lim, Revealing hot tearing mechanism for an additively manufactured high-entropy alloy via

selective laser melting, Scr. Mater. 168 (2019) 129–133.

https://doi.org/10.1016/j.scriptamat.2019.04.036.

[8]   S. Chandra, X. Tan, R.L. Narayan, C. Wang, S.B. Tor, G. Seet, A generalised hot

cracking criterion for nickel-based superalloys additively manufactured by

electron beam melting, Addit. Manuf. 37 (2021) 101633.

https://doi.org/10.1016/j.addma.2020.101633.

[9]   M. Awd, J. Tenkamp, M. Hirtler, S. Siddique, M. Bambach, F. Walther,

Comparison of microstructure and mechanical properties of Scalmalloy®

produced by selective laser melting and laser metal deposition, Materials

(Basel). 11 (2017). https://doi.org/10.3390/ma11010017.

[10]   K. Schmidtke, F. Palm, A. Hawkins, C. Emmelmann, Process and mechanical

properties: Applicability of a scandium modified Al-alloy for laser additive

manufacturing, Phys. Procedia. 12 (2011) 369–374.

https://doi.org/10.1016/j.phpro.2011.03.047.

[11]   A.B. Spierings, K. Dawson, M. Voegtlin, F. Palm, P.J. Uggowitzer,

Microstructure and mechanical properties of as-processed scandium-

modified aluminium using selective laser melting, CIRP Ann. - Manuf.

Technol. 65 (2016) 213–216. https://doi.org/10.1016/j.cirp.2016.04.057.

[12]   H. Zhang, D. Gu, J. Yang, D. Dai, T. Zhao, C. Hong, A. Gasser, R. Poprawe,

Selective laser melting of rare earth element Sc modified aluminum alloy:

Thermodynamics of precipitation behavior and its influence on mechanical

properties, Addit. Manuf. 23 (2018) 1–12.

https://doi.org/10.1016/j.addma.2018.07.002.

[13]   S. Lathabai, P.G. Lloyd, The effect of scandium on the microstructure,

mechanical properties and weldability of a cast Al-Mg alloy, Acta Mater. 50 (2002) 4275–4292. https://doi.org/10.1016/S1359-6454(02)00259-8.

[14] H. Zhang, H. Zhu, X. Nie, J. Yin, Z. Hu, X. Zeng, Effect of Zirconium addition on crack, microstructure and mechanical behavior of selective laser melted Al-Cu-Mg alloy, Scr. Mater. 134 (2017) 6–10. https://doi.org/https://doi.org/10.1016/j.scriptamat.2017.02.036.

[15] Q. Jia, P. Rometsch, S. Cao, K. Zhang, X. Wu, Towards a high strength aluminium alloy development methodology for selective laser melting, Mater. Des. 174 (2019) 107775. https://doi.org/https://doi.org/10.1016/j.matdes.2019.107775.

[16] S. Thapliyal, M. Komarasamy, S. Shukla, L. Zhou, H. Hyer, S. Park, Y. Sohn, R.S. Mishra, An integrated computational materials engineering-anchored closed-loop method for design of aluminum alloys for additive manufacturing, Materialia. 9 (2020) 100574. https://doi.org/10.1016/j.mtla.2019.100574.

[17] K. V. Yang, Y. Shi, F. Palm, X. Wu, P. Rometsch, Columnar to equiaxed transition in Al-Mg(-Sc)-Zr alloys produced by selective laser melting, Scr. Mater. 145 (2018) 113–117. https://doi.org/10.1016/j.scriptamat.2017.10.021.

[18] Y. Shi, K. Yang, S.K. Kairy, F. Palm, X. Wu, P.A. Rometsch, Effect of platform temperature on the porosity, microstructure and mechanical properties of an Al–Mg–Sc–Zr alloy fabricated by selective laser melting, Mater. Sci. Eng. A. 732 (2018) 41–52. https://doi.org/10.1016/j.msea.2018.06.049.

[19] J.R. Croteau, S. Griffiths, M.D. Rossell, C. Leinenbach, C. Kenel, V. Jansen, D.N.

Seidman, D.C. Dunand, N.Q. Vo, Microstructure and mechanical properties of Al-Mg-Zr alloys processed by selective laser melting, Acta Mater. 153 (2018) 35–44. https://doi.org/10.1016/j.actamat.2018.04.053.

[20] Q. Tan, J. Zhang, Q. Sun, Z. Fan, G. Li, Y. Yin, Y. Liu, M.-X. Zhang, Inoculation Treatment of an Additively Manufactured 2024 Aluminium Alloy with Titanium Nanoparticles, SSRN Electron. J. (2020). https://doi.org/10.2139/ssrn.3592041.

[21] C.A. Biffi, P. Bassani, J. Fiocchi, M. Albu, A. Tuissi, Selective laser melting of AlCu-TiB2 alloy using pulsed wave laser emission mode: processability, microstructure and mechanical properties, Mater. Des. 204 (2021) 109628. https://doi.org/https://doi.org/10.1016/j.matdes.2021.109628.

[22] A. Association, Aluminum: properties and physical metallurgy, ASM international, 1984.

[23] O. Gharbi, D. Jiang, D.R. Feenstra, S.K. Kairy, Y. Wu, C.R. Hutchinson, N. Birbilis, On the corrosion of additively manufactured aluminium alloy AA2024 prepared by selective laser melting, Corros. Sci. 143 (2018) 93–106. https://doi.org/10.1016/j.corsci.2018.08.019.

[24] Q. Tan, Y. Liu, Z. Fan, J. Zhang, Y. Yin, M.-X. Zhang, Effect of processing parameters on the densification of an additively manufactured 2024 Al alloy, J. Mater. Sci. Technol. 58 (2020) 34–45.

[25] P. Mair, V.S. Goettgens, T. Rainer, N. Weinberger, I. Letofsky-Papst, S. Mitsche, G. Leichtfried, Laser powder bed fusion of nano-CaB6 decorated 2024 aluminum alloy, J. Alloys Compd. 863 (2021) 158714. https://doi.org/10.1016/j.jallcom.2021.158714.

[26] M. Rasch, J. Heberle, M.A. Dechet, D. Bartels, M.R. Gotterbarm, L. Klein, A. Gorunov, J. Schmidt, C. Körner, W. Peukert, M. Schmidt, Grain structure evolution of Al-Cu alloys in powder bed fusion with laser beam for excellent mechanical properties, Materials (Basel). 13 (2020). https://doi.org/10.3390/ma13010082.

[27] X. Zhong, C.A. Wade, P.J. Withers, X. Zhou, C. Cai, S.J. Haigh, M.G. Burke, Comparing Xe+pFIB and Ga+FIB for TEM sample preparation of Al alloys: Minimising FIB-induced artefacts, J. Microsc. (2020) 1–12. https://doi.org/10.1111/jmi.12983.

[28] J.O. Andersson, T. Helander, L. Höglund, P. Shi, B. Sundman, Thermo-Calc & DICTRA, computational tools for materials science, Calphad Comput. Coupling Phase Diagrams Thermochem. 26 (2002) 273–312. https://doi.org/10.1016/S0364-5916(02)00037-8.

[29] Thermo-Calc, TCAL6: TCS Al-based Allot Database, (2019). https://thermocalc.com/products/databases/aluminum-based-alloys/.

[30] N. Kaufmann, M. Imran, T.M. Wischeropp, C. Emmelmann, S. Siddique, F. Walther, Influence of process parameters on the quality of aluminium alloy en AW 7075 using Selective Laser Melting (SLM), Phys. Procedia. 83 (2016) 918–926. https://doi.org/10.1016/j.phpro.2016.08.096.

[31] R. Pokharel, L. Balogh, D.W. Brown, B. Clausen, G.T. Gray, V. Livescu, S.C. Vogel, S. Takajo, Signatures of the unique microstructure of additively manufactured steel observed via diffraction, Scr. Mater. 155 (2018) 16–20. https://doi.org/10.1016/j.scriptamat.2018.06.008.

[32] G. Li, S.D. Jadhav, A. Martín, M.L. Montero-Sistiaga, J. Soete, M.S. Sebastian,

C.M. Cepeda-Jiménez, K. Vanmeensel, Investigation of Solidification and Precipitation Behavior of Si-Modified 7075 Aluminum Alloy Fabricated by Laser-Based Powder Bed Fusion, Metall. Mater. Trans. A Phys. Metall. Mater. Sci. 52 (2021) 194–210. https://doi.org/10.1007/s11661-020-06073-9.

[33] S. Kou, Welding metallurgy, New Jersey, USA. (2003) 431–446.

[34] R.W. Messler Jr, Principles of welding: processes, physics, chemistry, and metallurgy, John Wiley & Sons, 2008.

[35] N.T. Aboulkhair, N.M. Everitt, I. Ashcroft, C. Tuck, Reducing porosity in AlSi10Mg parts processed by selective laser melting, Addit. Manuf. 1–4 (2014) 77–86.

https://doi.org/https://doi.org/10.1016/j.addma.2014.08.001.

[36] L.P. Connor, Welding Metallurgy, Weld. Handb. (1987) 89–124.

https://doi.org/10.1007/978-1-349-10624-0_4.

[37] L. Katgerman, D.G. Eskin, In search of the prediction of hot cracking in aluminium alloys, in: Hot Crack. Phenom. Welds II, Springer, 2008: pp. 11–26.

[38] E. Scheil, Bemerkungen zur schichtkristallbildung, Int. J. Mater. Res. 34 (1942) 70–72.

[39] N.A. Ahmad, A.A. Wheeler, W.J. Boettinger, G.B. McFadden, Solute trapping and solute drag in a phase-field model of rapid solidification, Phys. Rev. E. 58 (1998) 3436–3450. https://doi.org/10.1103/PhysRevE.58.3436.

[40] M.J. Aziz, Model for solute redistribution during rapid solidification, J. Appl. Phys. 53 (1982) 1158–1168. https://doi.org/10.1063/1.329867.

[41] M.J. Aziz, An atomistic model of solute trapping, Rapid Solidif. Process. Princ.

Technol. III. (1982) 113–117.

[42]   M.J. Aziz, T. Kaplan, Continuous growth model for interface motion during

alloy solidification, Acta Metall. 36 (1988) 2335–2347.

https://doi.org/https://doi.org/10.1016/0001-6160(88)90333-1.

[43]   U. Scipioni Bertoli, B.E. MacDonald, J.M. Schoenung, Stability of cellular

microstructure in laser powder bed fusion of 316L stainless steel, Mater. Sci.

Eng. A. 739 (2019) 109–117. https://doi.org/10.1016/j.msea.2018.10.051.

[44]   F.H. Froes, Y.-W. Kim, S. Krishnamurthy, Rapid solidification of lightweight

metal alloys, Mater. Sci. Eng. A. 117 (1989) 19–32.

[45]   S. Kou, A criterion for cracking during solidification, Acta Mater. 88 (2015)

366–374.

[46]   T.W. Clyne, C. TW, The influence of composition on solidification cracking

susceptibility in binary alloy systems, (1981).

[47]   M. Rappaz, J.-M. Drezet, M. Gremaud, A new hot-tearing criterion, Metall.

Mater. Trans. A. 30 (1999) 449–455.

[48]   D.G. Eskin, Suyitno, L. Katgerman, Mechanical properties in the semi-solid

state and hot tearing of aluminium alloys, Prog. Mater. Sci. 49 (2004) 629–

711. https://doi.org/https://doi.org/10.1016/S0079-6425(03)00037-9.

[49]   S. Kou, A simple index for predicting the susceptibility to solidification

cracking, Weld. J. 94 (2015) 374s–388s.

[50]   N. Coniglio, C.E. Cross, Mechanisms for solidification crack initiation and

growth in aluminum welding, Metall. Mater. Trans. A. 40 (2009) 2718–2728.

[51]   M.L. Montero Sistiaga, R. Mertens, B. Vrancken, X. Wang, B. Van Hooreweder,

J.P. Kruth, J. Van Humbeeck, Changing the alloy composition of Al7075 for

better processability by selective laser melting, J. Mater. Process. Technol.

238 (2016) 437–445. https://doi.org/10.1016/j.jmatprotec.2016.08.003.

[52]   C. Hagenlocher, D. Weller, R. Weber, T. Graf, Analytical Description of the

Influence of the Welding Parameters on the Hot Cracking Susceptibility of

Laser Beam Welds in Aluminum Alloys, Metall. Mater. Trans. A Phys. Metall.

Mater. Sci. 50 (2019) 5174–5180. https://doi.org/10.1007/s11661-019-

05430-7.

[53]   J.M. Drezet, M.S.F. Lima, J.D. Wagnière, M. Rappaz, W. Kurz, Crack-free

aluminium alloy welds using a twin laser process, Weld. World. 52 (2008)

87–94.

[54]   M. Tang, P.C. Pistorius, S. Narra, J.L. Beuth, Rapid Solidification: Selective

Laser Melting of AlSi10Mg, Jom. 68 (2016) 960–966.

https://doi.org/10.1007/s11837-015-1763-3.

[55]   H. Matyja, The effect of cooling rate on the dendrite spacing in splat-cooled

aluminium alloys, J. Inst. Met. 96 (1968) 30–32.

[56]   M.C.H. Karg, B. Ahuja, S. Wiesenmayer, S.V. Kuryntsev, M. Schmidt, Effects of

process conditions on the mechanical behavior of aluminium wrought alloy

EN AW-2219 (AlCu6Mn) additively manufactured by laser beam melting in

powder bed, Micromachines. 8 (2017) 1–11.

https://doi.org/10.3390/mi8010023.

[57]   H. Zhang, H. Zhu, T. Qi, Z. Hu, X. Zeng, Selective laser melting of high strength

Al-Cu-Mg alloys: Processing, microstructure and mechanical properties,

Mater. Sci. Eng. A. 656 (2016) 47–54.

https://doi.org/10.1016/j.msea.2015.12.101.

[58] P. Wang, C. Gammer, F. Brenne, K.G. Prashanth, R.G. Mendes, M.H. Rümmeli, T. Gemming, J. Eckert, S. Scudino, Microstructure and mechanical properties of a heat-treatable Al-3.5Cu-1.5Mg-1Si alloy produced by selective laser melting, Mater. Sci. Eng. A. 711 (2018) 562–570. https://doi.org/10.1016/j.msea.2017.11.063.

[59] M. M'hamdi, A. Mo, H.G. Fjær, TearSim: A two-phase model addressing hot tearing formation during aluminum direct chill casting, Metall. Mater. Trans. A Phys. Metall. Mater. Sci. 37 (2006) 3069–3083. https://doi.org/10.1007/s11661-006-0188-6.

[60] A.A. Griffith, G.I. Taylor, VI. The phenomena of rupture and flow in solids, Philos. Trans. R. Soc. London. Ser. A, Contain. Pap. a Math. or Phys. Character. 221 (1921) 163–198. https://doi.org/10.1098/rsta.1921.0006.

[61] E. Orowan, Fracture and strength of solids, Reports Prog. Phys. 12 (1949) 185.

[62] J. Pelleg, Mechanical properties of materials, Springer Science & Business Media, 2012.

[63] M.F. Ashby, D. Cebon, Materials selection in mechanical design, Le J. Phys. IV. 3 (1993) C7-1.

[64] P. Mercelis, J.P. Kruth, Residual stresses in selective laser sintering and selective laser melting, Rapid Prototyp. J. 12 (2006) 254–265. https://doi.org/10.1108/13552540610707013.

[65] L.A. Parry, Investigation of Residual Stress, (n.d.).

[66] T. Mukherjee, W. Zhang, T. DebRoy, An improved prediction of residual stresses and distortion in additive manufacturing, Comput. Mater. Sci. 126

(2017) 360–372. https://doi.org/10.1016/j.commatsci.2016.10.003.

[67] D. Buchbinder, W. Meiners, N. Pirch, K. Wissenbach, J. Schrage, Investigation on reducing distortion by preheating during manufacture of aluminum components using selective laser melting, J. Laser Appl. 26 (2014) 12004.

[68] Z. Sun, X. Tan, C. Wang, M. Descoins, D. Mangelinck, S.B. Tor, E.A. Jägle, S. Zaefferer, D. Raabe, Reducing hot tearing by grain boundary segregation engineering in additive manufacturing: example of an AlxCoCrFeNi high-entropy alloy, Acta Mater. 204 (2021) 116505. https://doi.org/https://doi.org/10.1016/j.actamat.2020.116505.

[69] E. Chauvet, P. Kontis, E.A. Jägle, B. Gault, D. Raabe, C. Tassin, J.-J. Blandin, R. Dendievel, B. Vayre, S. Abed, G. Martin, Hot cracking mechanism affecting a non-weldable Ni-based superalloy produced by selective electron Beam Melting, Acta Mater. 142 (2018) 82–94. https://doi.org/https://doi.org/10.1016/j.actamat.2017.09.047.

[70] J.N. Ghoussoub, Y.T. Tang, C. Panwisawas, A. Németh, R.C. Reed, On the Influence of Alloy Chemistry and Processing Conditions on Additive Manufacturability of Ni-Based Superalloys, Miner. Met. Mater. Ser. (2020) 153–162. https://doi.org/10.1007/978-3-030-51834-9_15.

[71] L. Li, R. Li, T. Yuan, C. Chen, Z. Zhang, X. Li, Microstructures and tensile properties of a selective laser melted Al–Zn–Mg–Cu (Al7075) alloy by Si and Zr microalloying, Mater. Sci. Eng. A. 787 (2020) 139492. https://doi.org/10.1016/j.msea.2020.139492.

[72] M.J. Benoit, S.M. Zhu, T.B. Abbott, M.A. Easton, Evaluation of the Effect of Rare Earth Alloying Additions on the Hot Tearing Susceptibility of Aluminum

Alloy 7150 During Rapid Solidification, Metall. Mater. Trans. A Phys. Metall. Mater. Sci. 51 (2020) 5213–5227. https://doi.org/10.1007/s11661-020-05930-x.

[73]   N. Afzal, T. Shah, R. Ahmad, Microstructural features and mechanical properties of artificially aged AA2024, Strength Mater. 45 (2013) 684–692. https://doi.org/10.1007/s11223-013-9504-8.

Appendix A

A Matlab script, able to analyse defects based on image segmentation, was developed. Using this approach, each micrograph was converted into grey scale and then binarized to highlight the defects (in black) from the solidified alloy (in white). The material's relative density was computed by considering the ratio of the number of black pixels to the total number of pixels of the micrograph. The various defects were classified taking into account the geometrical features listed in Table A.1.

Table A.1: Geometrical features of each defect type identified by the Matlab routine.

Property Name	Symbol	Description
Circularity	C	Roundness of the region, evaluated by $\frac{4 \cdot Area \cdot \pi}{Perimeter^2}$. For a perfect circle, the circularity value is 1.
Major Axis Length	d_{max}	Length of the major axis of the ellipse that has the same normalized second central moments as the region.
Minor Axis Length	d_{min}	Length of the minor axis of the ellipse that has the same normalized second central moment as the region.
Orientation	φ	Angle between the horizontal axis and the major axis of the ellipse that has the same second-moment as the region.
Max Feret Diameter	$d_{max,f}$	Maximum distance between any two boundary points on the antipodal vertices of the convex hull that encloses the object.
Min Feret Diameter	$d_{min,f}$	Minimum distance between any two boundary points on the antipodal vertices of the convex hull that encloses the object.

In order to differentiate cracks and pores several geometrical constraints were applied to each feature. Defects satisfying the conditions expressed in Equation A.1 were treated as cracks:

$$C \leq 0.9 \; ; \quad \frac{d_{max,f}}{d_{min,f}} \geq 2 \; ; \quad |\varphi| \geq 45° \tag{A.1}$$

All the other defects were treated as pores. Depending on pore size, it was then possible to differentiate macro-pores, derived from lack-of-fusion or keyholing, from gas pores. Specifically, porosity satisfying the condition expressed in Equation A.2 was treated as gas porosity.

$$\frac{d_{max} + d_{min}}{2} \leq 0.05 \; mm \tag{A.2}$$

The remaining pores were categorised as lack-of-fusion and keyhole pores. Defects having a circularity of less than 0.9 were classified as lack-of-fusion. The remaining were classified as keyhole pores.

To quantify crack density, a cumulative crack length (CCL) parameter was used. CCL is defined as:

$$CCL = \frac{\sum_{i=1}^{N} d_{max,i}}{A} \tag{A.3}$$

where i is used to index the N cracks found in each micrograph where A is the total area of the micrograph and equals 7.11 mm^2. For each combination of laser power and speed experimentally analysed, four different micrographs were investigated to ensure a good level of repeatability in the measurements. Additionally, linear

interpolation between experimental points was carried out to better identify

trends between process parameters and recorded defects.